



JGR Atmospheres

RESEARCH ARTICLE

10.1029/2025JD043936

Special Collection:

Climate and weather extremes in a warming climate: Processes, Prediction and Projection

Key Points:

- Indian Ocean Dipole (IOD)'s climatic effect on southeastern Australia (SEA) is not stable and has been enhanced in recent decades
- IOD-induced severe bushfires risk has increased by 16%–32% due to anthropogenic climate change
- SEA will inevitably face an increasing crisis with bushfire in a warmer future

Supporting Information:

Supporting Information may be found in the online version of this article.

Correspondence to:

J. Huang, hjp@lzu.edu.cn

Citation:

Wang, S., Huang, J., Pang, Y., Li, X., Hu, Y., & He, Y. (2025). Intensifying climatic effects of the Indian Ocean dipole exaggerates Australia bushfires risk. *Journal of Geophysical Research: Atmospheres*, *130*, e2025JD043936. https://doi.org/10.1029/2025JD043936

Received 21 MAR 2025 Accepted 28 AUG 2025

Intensifying Climatic Effects of the Indian Ocean Dipole Exaggerates Australia Bushfires Risk

Shanshan Wang¹, Jianping Huang¹, Yiwei Pang¹, Xiaoping Li¹, Yuanyuan Hu¹, and Yongli He¹

¹Key Laboratory for Semi-Arid Climate Change of the Ministry of Education, College of Atmospheric Sciences, Lanzhou University, Lanzhou, China

Abstract Southeastern Australia (SEA) is no stranger to bushfires, but the 2019–2020 season was unprecedented in both size and intensity, accompanied with record-breaking high temperature and rainfall deficit. Future projections warn that Australia's fire season will face more frequent droughts and heat waves if emissions are not significantly reduced. Although studies have indicated 2019 extreme positive Indian Ocean Dipole's (pIOD) important contribution to this mega bushfire, our research study highlights IOD's climatic effect on SEA varied and intensified in recent decades. Due to anthropogenic climate change, the likelihood of pIOD-induced severe bushfires danger has risen by 16%–32%. Coupled Model Intercomparison Project Phase 6 projections reveal that SEA will inevitably face an increasing crisis with bushfire in a warmer future. Under the plausible high-emission scenario SSP370, pIOD-induced mega bushfires comparable to the 2019–2020 event increase at nearly 1.8 times the rate of medium-emission SSP245, whereas the upper-bound SSP585 scenario projects over twice SSP245's increase.

Plain Language Summary Bushfires are not uncommon in Australia due to its extensive grasslands and large semi-arid landscapes, but the 2019–2020 season in southeastern Australia (SEA) has been proved to be unprecedented in both scale and intensity due to unusually hot and dry conditions, which was driven by a climate event called the positive Indian Ocean Dipole (pIOD). Our study reveals that IOD's climatic effect on SEA is not stable and enhanced in recent decades. The likelihood of severe bushfires danger driven by pIOD has increased by about 16%–32% due to anthropogenic climate change. Projections using Coupled Model Intercomparison Project Phase 6 shows that the effects of pIOD will likely become stronger, leading to even more extreme fire-prone conditions by the late 21st century. Under the plausible high-emission scenario SSP370, pIOD-induced mega bushfires comparable to the 2019–2020 event increase at nearly 1.8 times the rate of medium-emission SSP245, whereas the upper-bound SSP585 scenario projects over twice SSP245's increase. Our findings highlight the urgent need to develop effective strategies and plans to mitigate the glowing threat of bushfires over Australia.

1. Introduction

Bushfires are not uncommon in Australia due to the extensive grasslands and the large semi-arid landscape, which have a substantial impact on environmental, social, and economy, but the 2019–2020 season in southeastern Australia (SEA) was unprecedented in its scale and intensity, attracting considerable national and international attention (Boer et al., 2020; Nolan et al., 2020). These deadly bushfires that began in September 2019 were burning for nearly four months and turned eastern Australia into a charred apocalyptic nightmare. By mid-February 2020, more than 186,000 Km² of land were burned in thousands of fires, resulting in at least 34 fatalities. An estimated billion animals—800,000 in New South Wales alone—were killed. Nearly 3,000 homes and several thousand buildings were destroyed nationwide. The total damages of these bushfires were estimated at \$100 billion or more, making it Australia's costliest natural disaster in history (https://disasterphilanthropy.org/disaster/2019-australian-wildfires). This catastrophic event highlights the critical need to better understand the climatic drivers contributing to extreme fire seasons.

Prior to the 2019–2020 mega fires, Australia had experienced a prolonged period of hot and dry conditions over the past two years, and 2019 was the hottest and driest year on record for the country. These repeated warm days, little or no rain, combined with some periods of windy weather contributed to the unusual volatility of the 2019–2020 fire season (Deb et al., 2020). Studies have indicated that several interacting climatic factors contributed to the severity of the 2019–2020 fire season; the most notable triggers include a record-breaking positive Indian

© 2025. American Geophysical Union. All Rights Reserved.

WANG ET AL. 1 of 12

Ocean Dipole (pIOD), alongside the Central Pacific El Niño (CP-El Niño) and anthropogenic climate change (Abram et al., 2021; Di Virgilio et al., 2020; Van Oldenborgh et al., 2021; Wang & Cai, 2020). The IOD's impact on Australian precipitation and temperature is dynamically grounded in the Matsuno-Gill atmospheric response (Ashok et al., 2003). pIOD phases—characterized by warmer-than-average sea surface temperatures (SSTs) in the western Indian Ocean and cooler-than-average conditions in the eastern Indian Ocean—can induce anomalous subsidence over SEA and significantly impact the Australian climate (Cai et al., 2009). A pIOD phase often leads to reduced rainfall and warmer temperatures across eastern Australia, creating drought conditions. This drought significantly increases landscape flammability by dry vegetation, thereby providing substantial fuel for wildfires and thus increasing their vulnerability and spread (Cai et al., 2009, 2011; Dowdy et al., 2009; Ummenhofer et al., 2009).

However, we notice that the relationship between strong pIOD events and extreme fire weather in SEA is not invariably consistent. A strong pIOD does not always result in extreme heat and dryness with high fire potential in SEA. A notable example is 1961, which experienced the third strongest IOD since 1900, did not record a significant rainfall deficit or associated extreme fire impacts in SEA. This historical discrepancy raises critical questions about the stability of the pIOD's preconditioning influence on SEA drought and bushfire risk over time. Specifically, it prompts investigation into whether the teleconnection between pIOD and SEA climate/fire risk has undergone significant variations in recent decades, potentially modulated by anthropogenic climate change. To address the above questions, this study will investigate the varying pIOD's impact on SEA drought and fire risk in the historical and future contexts, which is essential for developing effective strategies and plans to mitigate the threat of bushfires in Australia.

2. Materials and Methods

2.1. Observational Materials

Modis active fire data (Collection 6, standard and near real time archives, available on https://firms.modaps.eosdis.nasa.gov/download/; Giglio et al., 2016) was used to provide a visual representation of the unprecedented scale of the 2019–2020 Australian mega-fires. Meteorological data, including daily maximum and minimum air temperature ($T_{\rm max}$ and $T_{\rm min}$) and precipitation were obtained from the Australian Gridded Climate Data set (AGCDv2; Evans et al., 2020), which is a high-quality, publicly available, and widely used data set produced by the Bureau of Meteorology (BOM, available at https://thredds.nci.org.au/thredds/catalog/catalogs/zv2/agcd/agcd.html). In addition, the NOAA's Precipitation Reconstruction (PREC; Chen et al., 2002) and outgoing longwave radiation (OLR) data from NCEP-NCAR Reanalysis 1 (Kalnay et al., 1996) from 1948 to 2020 were also incorporated. To fit the annual mean variables and estimate return periods, we employed the generalized extreme value (GEV) distribution in this study, which is appropriate for fitting the tails of data distributions (Coles et al., 2001)

To quantify the IOD events, which are known to significantly influence Australian climate variability and drought conditions (Cai et al., 2009), the Dipole Mode Index (DMI) was used. It was defined as the SST anomalies (SSTA) difference between the West Tropical Indian Ocean (WTIO, 50°–70°E, 10°S–10°N) and the Southeast Tropical Indian Ocean (SETIO, 90°–110°E) (Saji et al., 1999). The observed DMI was derived from the most recent version of the Extended Reconstruction of SST (ERSSTv5; Huang et al., 2017), providing a reliable index of IOD variability for the study period.

2.2. Computation of Keetch-Byram Drought Index

The Keetch-Byram drought index (KBDI; Keetch & Byram, 1968) was selected as the primary drought metric for this study due to its established utility in assessing fire risk, especially in the context of fuel aridity, which is known to be a critical driver of wildfire behavior. The KBDI represents the soil moisture deficit relative to soil capacity, providing a straightforward measure of the drying of surface fuels and their flammability. This index has been widely used in Australia (e.g., Plucinski et al., 2023) and globally (e.g., Gannon & Steinberg, 2021) for fire management as well as drought monitoring. It is calculated using a simple water balance calculation based on the BOM meteorological data for the period from 1900 to 2020. KBDI values range from 0 mm, indicating saturated soil, to 800 mm for extremely dry conditions. The calculation is shown in Equations 1 and 2:

WANG ET AL. 2 of 12

Table 1 List of CMIP6 Models Used in This Study

Models	his	hisnat	ssp245	ssp370	ssp585
ACCESS-ESM1-5	3	3	3	3	3
ACCESS-CM2	3	3	3	3	3
CanESM5	10	10	10	10	10
CNRM-CM6-1	1	1	1	1	1
FGOALS-g3	3	3	3	3	3
GFDL- CM4	1	1	1	0	1
GFDL-ESM4	1	1	1	1	1
IPSL-CM6A-LR	5	6	5	5	5
MIROC6	50	50	50	50	50
MRI-ESM2-0	5	5	5	5	5
NorESM2-LM	1	3	1	1	1
11	83	86	83	82	83

Note. Numbers indicate the number of ensemble members for each experiment group in each model. The bold numbers in the last row represent the total number of experiments used.

$$\begin{aligned} \text{DF}_t &= \frac{[800 - \text{KBDI}_{t-1}] \left[0.968 \times e^{0.0875T\text{MAX}_t + 1.5552} - 0.83 \right]}{1 + 10.88e^{-0.00174R}} \times 10^{-3} \quad (1) \\ \text{KBDI}_t &= \text{KBDI}_{t-1} \text{ , if } P_t = 0\text{mm and } T\text{MAX}_t \leq 6.78\,^{\circ}\text{C} \\ \text{KBDI}_t &= \text{KBDI}_{t-1} + \text{DF}_t, \quad \text{if } P_t = 0\text{mm and } T\text{MAX}_t > 6.78\,^{\circ}\text{C} \\ \text{KBDI}_t &= \text{KBDI}_{t-1} + \text{DF}_t, \quad \text{if } P_t > 0\text{mm and } \sum P_t \leq 5.1\text{mm} \\ \text{KBDI}_t &= \text{KBDI}_{t-1} - 39.37 \sum P_t + \text{DF}_t, \quad \text{if } P_t > 0\text{mm and } \sum P_t > 5.1\text{mm} \end{aligned}$$

Where DF is the drought factor and represents the drought increment on a given day (Janis et al., 2002), $TMAX_t$ and P_t are daily maximum temperature (°C) and precipitation (mm), respectively, R is the average annual rainfall in the region (mm), and $KBDI_{t-1}$ is the Keetch-Byram drought index for time t-1 (the day before) (Janis et al., 2002; Salehnia et al., 2018). The KBDI is initialized after several consecutive rainy days reaching soil saturation, typically at 150 mm of cumulative precipitation in our study area, following the suggestions by Keetch and Byram (1968).

2.3. Model Simulations and Analysis

We utilized daily historical simulations (1900-2014) and future projections (2015-2100) from the Coupled Model Intercomparison Project Phase 6 (CMIP6; Eyring et al., 2016) under various shared socioeconomic pathways (SSPs, including SSP245, SSP370 and SSP585) in this study (see Table 1 for the model list and information). The selection of CMIP6 models was carefully considered, acknowledging the varying performance characteristics demonstrated in the literature, with a focus on studies specific to the Australian climate (Di Virgilio et al., 2022; Grose et al., 2020, 2023). Model selection included consideration of both overall performance in simulating Australian climate variables and the diversity of climate change signals generated by each model. All simulations were bilinearly regridded into 0.5° resolution and matched well with the observed distribution via a Kolmogorov-Smirnov test (p < 0.05).

To quantitatively assess the contributions of anthropogenic influence on Australia's 2019–2020 mega-bushfires, the probability ratio (PR; Fischer & Knutti, 2015) was calculated using the definition of PR = $P_{\rm ALI}/P_{\rm NAT}$. Here, P_{NAT} denotes the probability of exceeding the defined threshold under natural-forcing scenarios and P_{ALL} represents the equivalent under the all-forcings scenarios. Bootstrapping was performed 1,000 times to estimate the PR uncertainty of PR through resampling (Du et al., 2021; Wang et al., 2019; Yuan and Hu, 2018).

3. Results

3.1. Weather Conditions of 2019-2020 Bushfires

The bushfires sparked in September 2019, but the story really began back in 2017 (Wang & Cai, 2020). This prolonged drought set the stage for an especially severe bushfire season in SEA, including the eastern parts of the New Wales and Victoria, which suffered the greatest impact (Figure 1a). In addition to 2019 being the driest year on record since 1900, it was also Australia's warmest year (Figures 1b-1e). In 2019, the annual mean temperature was 1.52°C above the average. Especially from spring to early summer (September–January), most of eastern Australia was endured severe hot weather, with temperature anomalies up to 4°C (Figures 2a and 2b). Unlike the nationwide trend of increasing annual temperatures, the temperature in SEA from September to January has fluctuated on an interdecadal timescale, with a sharp increase observed over the past 70 years. The highest daily maximum temperature (TX) and the average for 7 consecutive days (Tx7x) in this region ranked third and fourth since 1900, respectively. During September 2019 to January 2020, the number of heatwave days (daily maximum temperature is greater than 35°C) reached 18, the most in 120 years of record-keeping. Throughout the same period, SEA experienced the direct spring to early summer on record. Under the joint effects of high temperatures and extreme precipitation deficits, the mean KBDI value from September 2019 to January 2020 reached the

WANG ET AL. 3 of 12

21698996, 2025, 18, Downloaded from https://agupubs.onlinelibrary.wiley.com/doi/10.1029/2025ID043936 by Lanzhou University, Wiley Online Library on [05/11/2025]. See the Terms

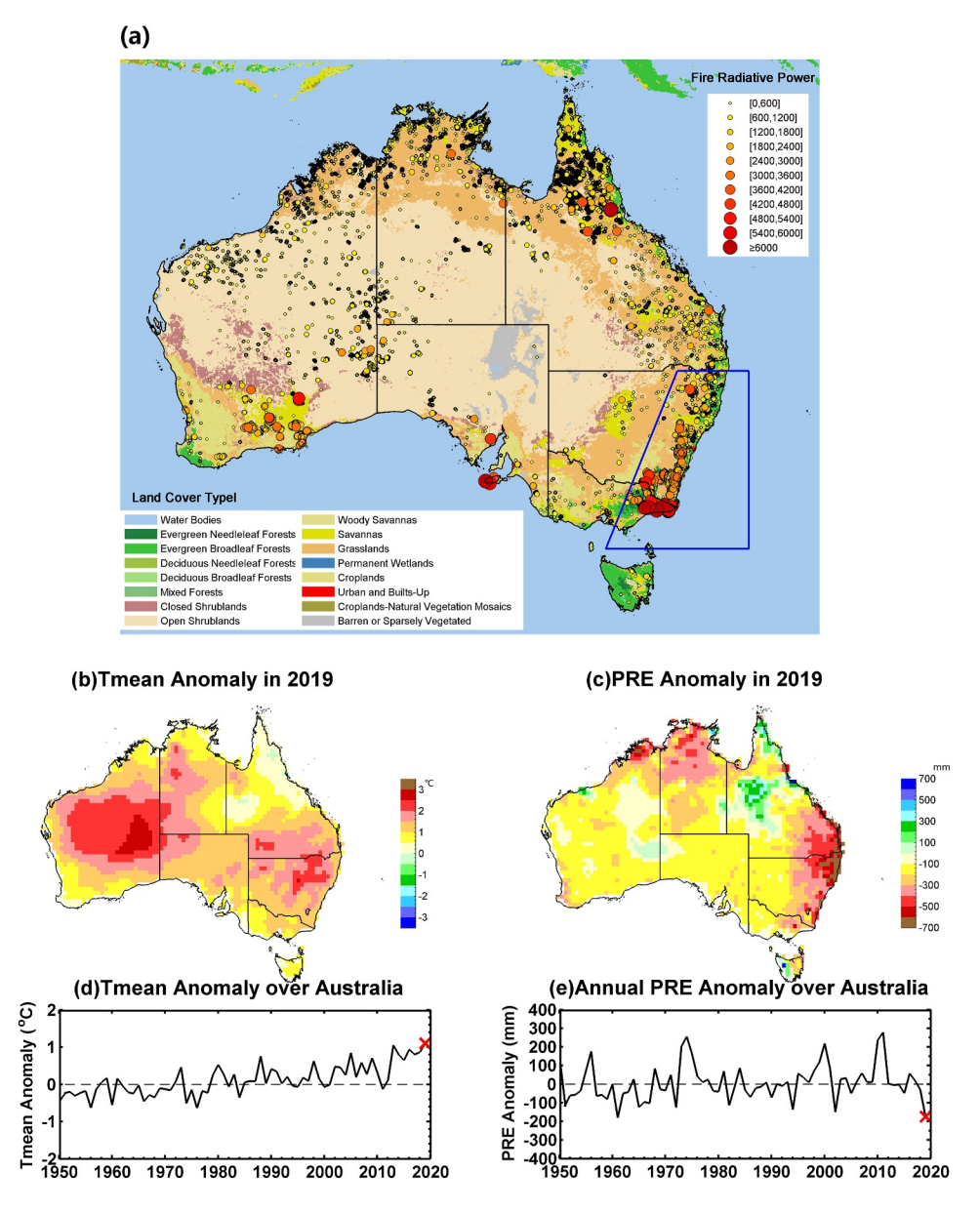


Figure 1. Modis active fire data (Collection 6, standard and near real time archives, available on https://firms.modaps.eosdis.nasa.gov/download/) during 1 September 2019–31 January 2020. The most severe fires were heavily concentrated in the temperate forests of southeastern Australia. The polygon region in blue is the studying area in this paper.

highest level ever recorded, indicating the highest fire potential and risk in SEA. Correspondingly, an anomalous high-pressure system characterized the atmospheric circulation around Australia, subjecting eastern Australia to anomalous sinking motions (Figure 3), thereby fostering persistent dry and hot weather conductive to fire activities. This anomalously anticyclonic circulation has been evidenced to be triggered by the pIOD–related cold SSTAs west of the Indonesian archipelago, consistent with the Matsuno-Gill theory (Ashok et al., 2003; Zhang et al., 2021).

3.2. Inter-Decadal Climatic Effect of IOD Increasing the Risk of Bushfires

Previous studies have indicated that pIOD events contribute to rainfall deficit and higher temperatures, thereby exacerbating dry conditions and increasing wildfire risk over SEA, particularly during the austral spring that is the mature time of the IOD (Cai et al., 2009), as indicated in Figure 4b. Our detrended correlation analysis between September–January precipitation, temperature and KBDI over SEA, and the simultaneous DMI corroborates this

WANG ET AL. 4 of 12

21698996, 2025, 18, Downloaded from https://agupubs.onlinelibrary.wiley.com/doi/10.1029/2025/D043936 by Lanzhou University, Wiley Online Library on [05/11/2025]. See the Terms and Conditions (https://onlinelibrary.wiley.com/erms-and-conditions) on Wiley Online Library for rules of use; OA articles

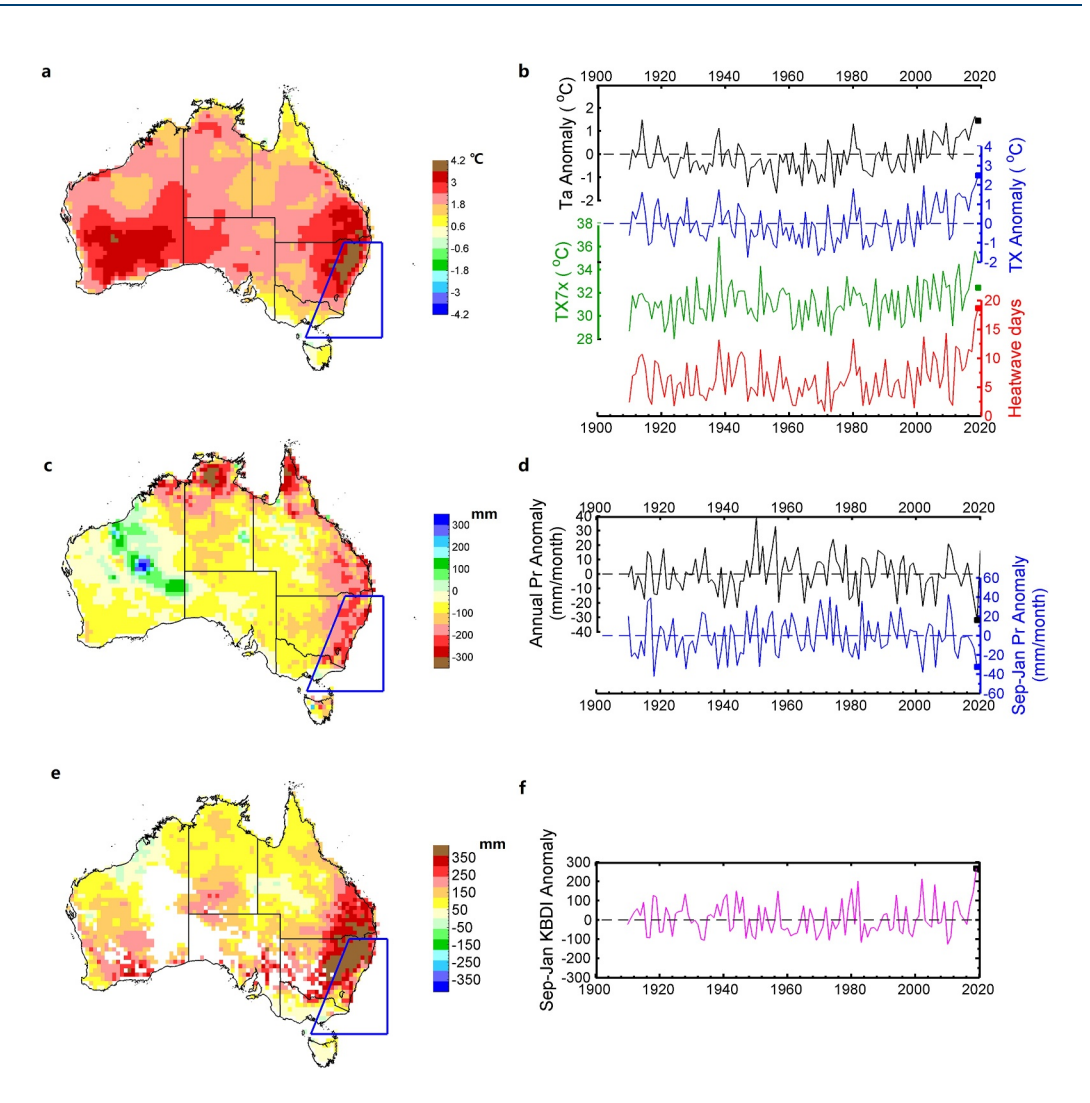


Figure 2. Spatial and temporal distribution of temperature, precipitation, and KBDI over southeastern Australia. Panel (a) maximum daily temperature ($T_{\rm max}$) anomaly (units: $^{\circ}$ C), (c) precipitation anomaly (units: mm), and (e) KBDI anomaly (units: mm) during 1 September 2019–31 January 2020; (b) the corresponding time series over southeast Australia in terms of the September–January mean temperature anomaly (in black, units: $^{\circ}$ C), the mean $T_{\rm max}$ anomaly (in blue; units: $^{\circ}$ C), the maximum average $T_{\rm max}$ for 7 consecutive days (TX7x, in green; units: $^{\circ}$ C), and the heatwave days (in red, units: day) since 1900. (d) Same as (b) but for the annual mean (in black; units: mm/month) and September–January mean (in blue; units: mm/month) precipitation anomaly over southeast Australia. (f) Time series of September–January mean KBDI averaged over southeast Australia. All anomalies are calculated with respect to the 1981–2010 base period. Here, heatwave days are defined as the days that is greater than 35°C during September to January in next year. The polygon region in blue is the studying area in this paper.

relationship. Specifically for the precipitation, there is a strong inverse correlation with the coefficient of -0.30 (pvalue < 0.01) for the entire 1900–2019 period (Figure 4a). However, we notice that this relationship is not stable and varies on inter-decadal time scale (Figure 5a). Using a 21-year sliding window with a 1-year interval (Sun et al., 2016), the anticorrelation becomes nonsignificant for the period 1928–1996 (corr. = -0.03, pvalue = 0.80). Before 1928 and after 1996, the correlations were statistically significant, with coefficients of -0.70 and -0.57, respectively. Importantly, the temporal dynamics of this IOD-precipitation relationship closely parallel the decadal variability observed in the IOD-NINO3.4 correlation (Figure 5d), suggesting a potential link between the changing IOD-El Niño relationship and the IOD's influence on SEA precipitation. The correlation patterns between September–January DMI and Australia precipitation in different subperiods highlight the interdacadal effects of IOD on SEA (Figures 6a–6c). Regressed precipitation data from NOAA's Precipitation Reconstruction (PREC, Figures 6d–6f) and outgoing longwave radiation (OLR, Figures 6g–6i) against September–January DMI support the conclusion that the impact of IOD on SEA's climate has enhanced in recent decades. Notably, this

WANG ET AL. 5 of 12

21698996, 2025, 18, Downloaded from https://agupubs.onlinelibrary.wiley.com/doi/10.1029/2025JD043936 by Lanzhou University, Wiley Online Library on [05/11/2025]

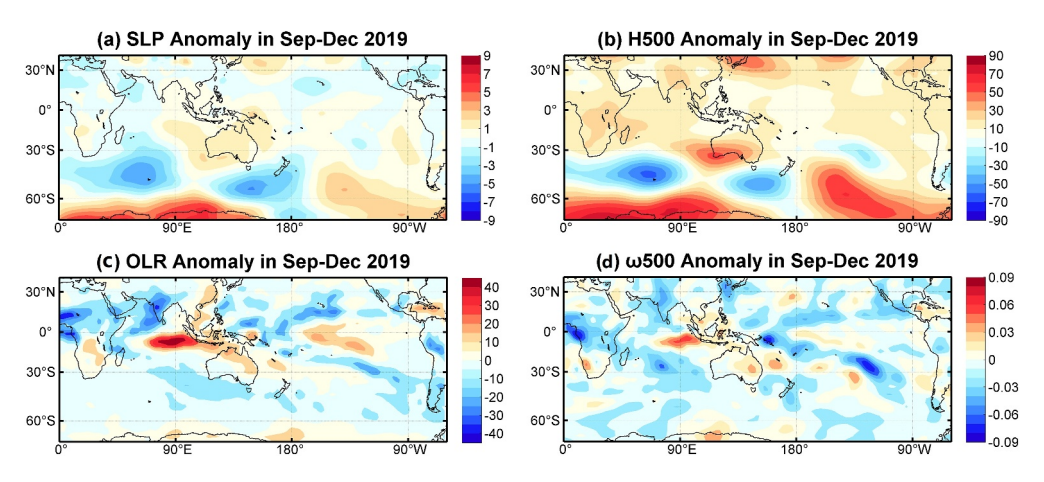


Figure 3. Seasonal mean circulation anomalies field during 1 September 2019–31 January 2020. (a) sea level pressure (SLP, unite: hPa); (b) geopotential height (H500, unit: gpm); (c) the outgoing longwave radiation (OLR, unit: $W \cdot m^{-2}$); (d) the vertical velocity (unit: pascal·s⁻¹). All anomalies are calculated with respect to the 1981–2010 base period.

enhanced impact demonstrates strong physical coherence—the observed precipitation anomalies (Figures 6d–6f) align with theoretical expectations of Gill-Matsuno responses to tropical SST forcing (Ashok et al., 2003)—affirming the physical basis of the IOD-KBDI causal chain. This enhanced effect, combined with the extreme pIOD event in 2019, significantly contributed to the 2019–2020 mega bushfire in SEA.

The relationship between DMI and temperature also shows interdecadal variability, which aligns with fluctuations in the amplitude of the DMI (Figures 5b and 5e). During the early 20th century and the last three decades, the anomalously high temperatures scorched SEA in pIOD years with large amplitudes. Regarding the KBDI which is influenced by both daily precipitation and maximum temperature, similar results to precipitation were observed. The relationship between KBDI and DMI was weak from 1928 to 1990, but significant correlation appeared before 1928 (*corr.* = 0.70, *pvalue* <<0.01) and after 1991 (*corr.* = 0.72, *pvalue* <<0.01), slightly differing from precipitation due to temperature's influence. Thus, we categorize 1928–1990 as a low-relationship period (termed as L) and 1991–2019 as a high-relationship period (termed as H).

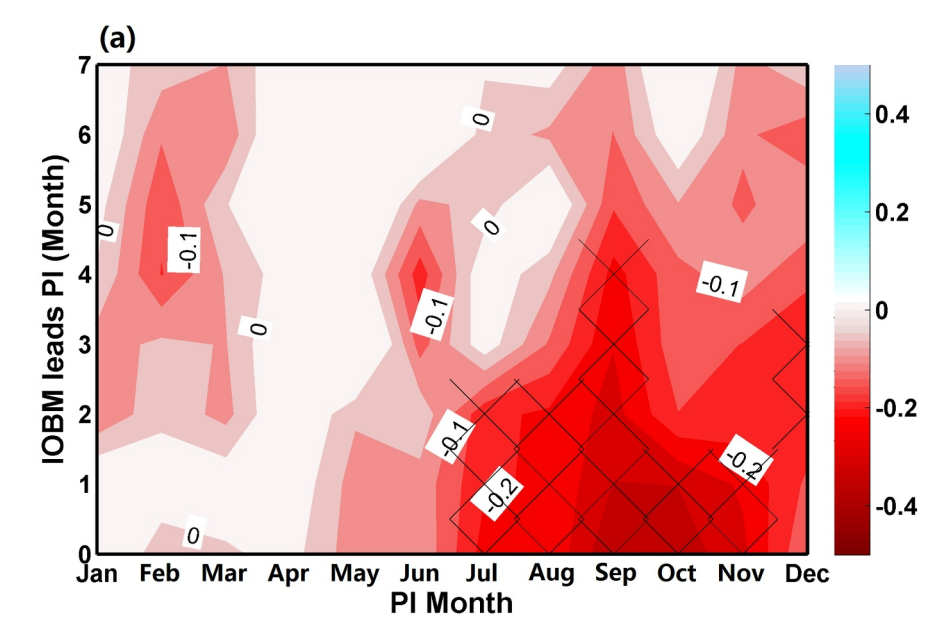
Comparing the probability density functions from the L- and H-period shows varying climate responses to IOD events across different subperiods (Figures 5g–5i). Since 1991, the GEV fit shows that the likelihood of extreme precipitation deficit over SEA like 2019–20 during pIOD years has increased from about 11.2% during the L-period to 21.6%. Such extreme dryness is a rare occurrence during a negative IOD (nIOD) event, with probability of 7.6% during the L-period, which has not occurred during the H-period. When comparing the climatic effects of pIOD and nIOD events, the likelihood of an extreme precipitation deficit in SEA—similar to that occurring from September to January in 2019–2020—has increased nearly fourfold over the past three decades (H-period) compared to L-period.

The effect of IOD on the KBDI aligns with its impact on precipitation. There is a significant shift in the KBDI toward much higher bushfire risk in pIOD years during the H-period (Figure 6i), with the likelihood of pIOD-induced extreme bushfire potential over SEA like 2019–2020 mega fire increasing from 4.3% during the L-period to 15.4% during the H-period. Such conditions rarely happen in nIOD years, with a 0.2% probability during the L-period and no occurrence in the past three decades (H-period). Overall, the probability of SEA experiencing extreme fire potential increased by pIODs (compared with that by nIOD) has raised by about 170% since 1991 compared to the period 1927–1990.

What causes the different effects of pIOD on SEA climate? Composite SSTA in September–January for the positive IOD events in different subperiods were further investigated (Figure 7). A key difference is that there were significantly warmer SSTs in the equatorial central and eastern Pacific before 1928 and after 1900. Notably, eight out of nine pIOD years are accompanied with El Niño events (defined as the September–January mean NINO34 index greater than 1s.d.) during both 1900–1927 and 1991–2019 (Figure S1). The only exception is the year of 2019 which was also a moderate Central Pacific El Niño (Ren et al., 2019). However, only three out of seven pIODs coincided with warmer SSTs in the equatorial central and eastern Pacific during 1928–1990. For

WANG ET AL. 6 of 12

21698996, 2025, 18, Downloaded from https://agupubs.onlinelibrary.wiley.com/doi/10.1029/2025ID043936 by Lanzhou University, Wiley Online Library on [05/11/2025]. See the Terms



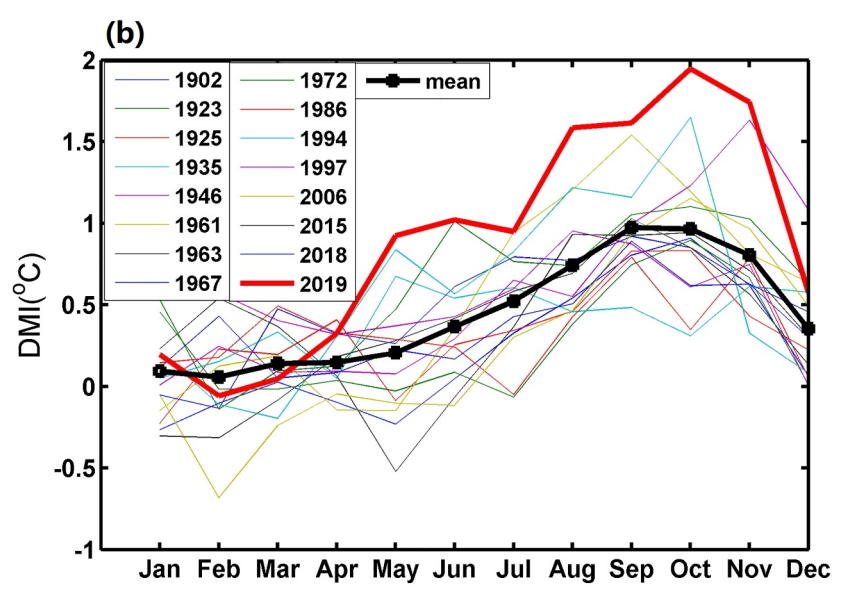


Figure 4. Relationship of Indian Ocean Dipole (IOD) and precipitation over Australia for the period of 1900–2019. (a) the monthly evolution of correlation coefficient of the IOD and precipitation over Australia and (b) the corresponding Dipole Mode Index seasonal evolutions in the positive IOD years. In panel (a), *x* axis is month of precipitation (PI) and *y* axis is the month of IOBM leading the precipitation; the striped region have passed the significant level at 0.05.

instance, the year 1961, with the third strongest IOD since 1900, occurred in the context of the SST anomalies in the tropical Indian Ocean and Pacific Ocean were dominated by cooler-than-average conditions (La Niña), which tend to increase rainfall over eastern Australia and offset the drying effects of positive IOD. Furthermore, between 1927 and 1990, the correlation between IOD and rainfall or temperature over eastern Australia was quite weak and insignificant, indicating that during this period, the influence of IOD on the Australian climate was limited. Cai et al. (2009, 2011) also noted that severe bushfires in SEA are more likely when preceded by a pIOD in conjunction with an El Niño. Further analyses confirm that the effect of IOD on precipitation typically strengthens when IOD is closely associated with the NINO34 index, suggesting that SEA experiences much drier conditions in spring-early summer when pIOD occurs with El Niño (Figure 5d).

WANG ET AL. 7 of 12

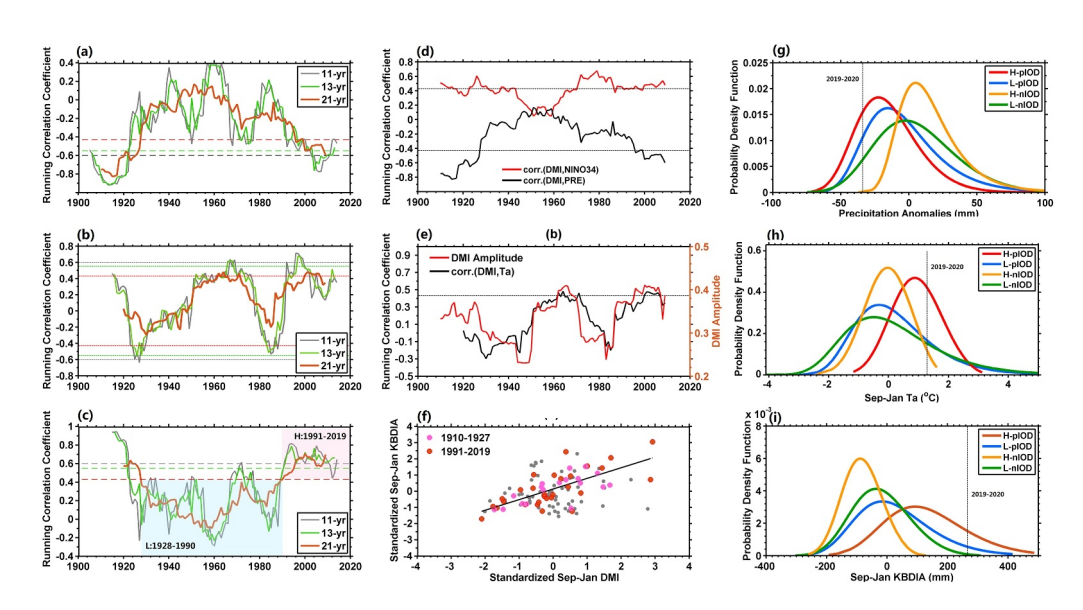


Figure 5. Relations of Indian Ocean Dipole (IOD) and Australia's climate. (a) Evolution of the 11-, 13-, and 21-year sliding correlation coefficient (*r*) between September–January Dipole Mode Index (DMI) and a precipitation. Panels (b) and (c) are same as (a), but for the mean temperature and KBDI over southeast Australia. Their confidence levels of 95% are shown as the dashed gray, green, and pink lines. (d) Evolution of the 21-year running correlation coefficients between DMI and precipitation (in dark) and NINO34 (in red). (e) Evolution of the 21-year running correlation coefficients between DMI and temperature (in dark) and DMI amplitude (in red). (f) Scatters of September–December mean DMI against the KBDI anomalies in the same period. (g)–(i) Probability density functions for (g) precipitation, (h) mean temperature and (i) KBDI in southeastern Australia during positive or negative IOD years under for the High-influence period (1991–2019, denoted as (h) and Low-influence period (1928–1990, denoted as L). The black dashed line is the observed value in 2019/2020.

3.3. Projected Risk in a Warming Future Climate

Recent projections of fire weather suggest that SEA is likely to become hotter and drier, thereby facing increased bushfire risk in future (Abram et al., 2021; Lucas et al., 2007). In this study, to quantitatively assess the influence of greenhouse warming on IOD's effect on extreme bushfire weather in SEA, we use CMIP6 multi-model database driven by historical anthropogenic and natural forcings, along with future Shared Socioeconomic Pathways (SSPs, including SSP245, SSP370 and SSP585), covering the period from 1900 to 2099 (see Table 1). Figures 8a and 8b display the time series of the September–January KBDI for SEA during both historical and future periods. In the historical period and first half of the 21st century, the increase in bushfire risk is not particularly evident (Figure 8a). However, entering into the mid-21st century, changes in bushfire risk become more significant, particularly under SSP585. Although there is no abrupt difference between the historical allforcing and nature only forcing throughout the historical period, a more rapid increase in KBDI compared to the natural forcing is observed in recent decades (Figure 8b).

A further GEV fitting shows that pIOD-induced severe bushfire events (above the 95th percentile) and extreme events (above the 99th percentile) has increased by about 24% (±8%) and 13% (±13%) due to anthropogenic climate change. In the future, the projected likelihood of severe and extreme bushfire events induced by IOD depicts a significant increase, especially for very extreme bushfire events such as that occurring in 2019–2020 in ESA (Figure 8d). The probability of extreme bushfire events related to nIOD events does not vary significantly under different SSPs. However, the impact of pIOD on SEA bushfire risk under SSP370 and SSP585 is notably enhanced compared to SSP245, with an overall shift of KBDI toward a much higher bushfire risk. During pIOD years, the probability of severe bushfires (95th percentile) rises from 28% under SSP245 to 37% under SSP370 and 42% under SSP585. Similarly, extreme bushfire risk (99th percentile) increases from 13% (SSP245) to 20% (SSP370) and 23% (SSP585). Notably, under the upper-bound SSP585 scenario, very extreme mega-fires comparable to that of the 2019–2020 event become 91%–149% more likely relative to SSP245.

A statistically positive relationship exists between inter-model variations in the IOD/ENSO correlation and inter-model variations in the IOD/KBDI correlation under historical-all forcing, suggesting that the IOD's effect on bushfire weather in SEA intensifies when the IOD/ENSO relationship strengthens. Under the influence of

WANG ET AL. 8 of 12

21698996, 2025, 18, Downloaded from https://agupubs.onlinelibrary.wiley.com/doi/10.1029/2025JD043936 by Lanzhou University, Wiley Online Library on [05/11/2025]. See the Terms and Conditions (https://onlinelibrary.wiley.com/erms

and-conditions) on Wiley Online Library for rules of use; OA articles are governed by the applicable Creative

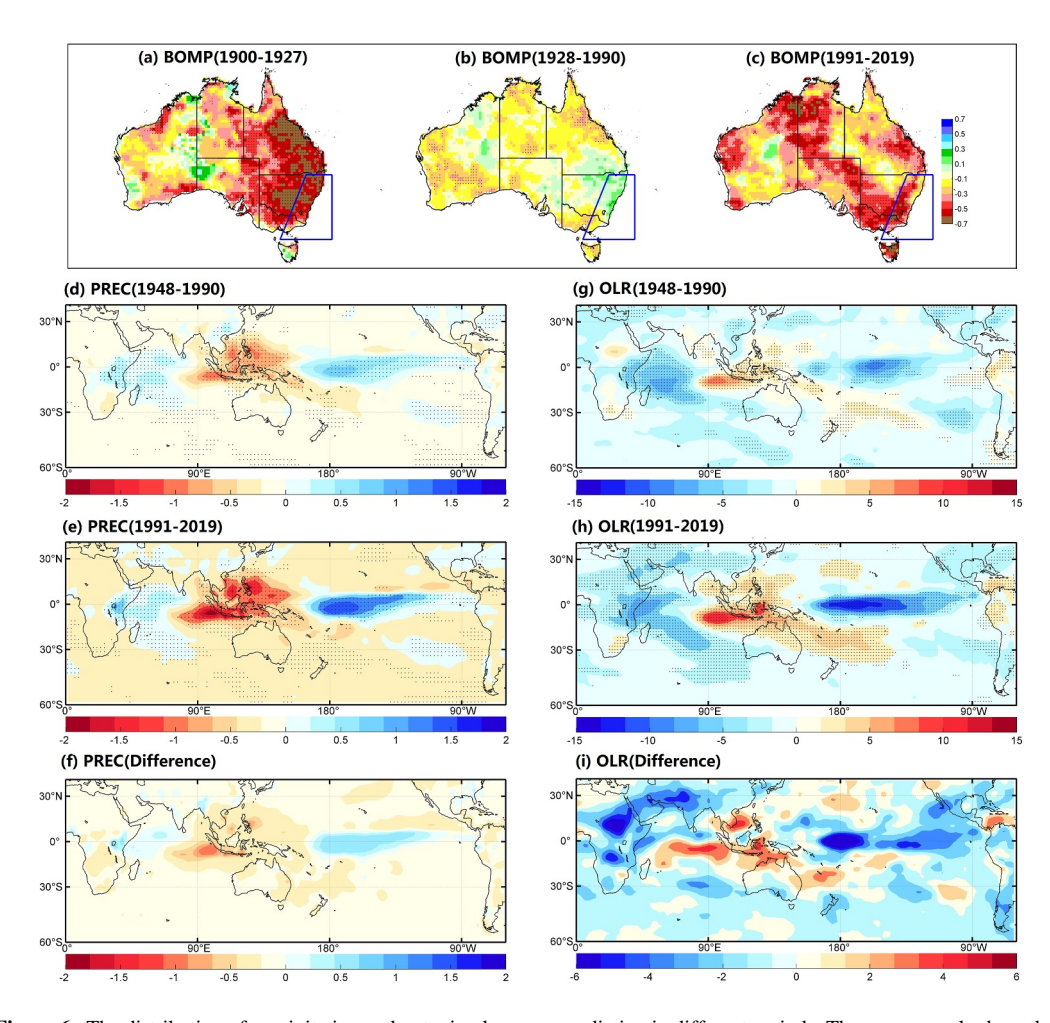


Figure 6. The distribution of precipitation and outgoing longwave radiation in different periods. The upper panels show the correlation coefficient between the September–January Dipole Mode Index and Bureau of Meteorology observed precipitation in the subperiods of (a) 1900–1927, (c) 1928–1990, and (c)1991–2019. (d) The precipitation (PRE, unit: mm/day) fields regressed against September–January mean IOBM for low-relationship period of 1948–1990 since the PREC precipitation data set started from 1948, (e) the high-relationship period of 1991–2019, and (f) their difference. (g–i) Same as (d–f), but for outgoing longwave radiation (OLR, unit: W·m⁻²).

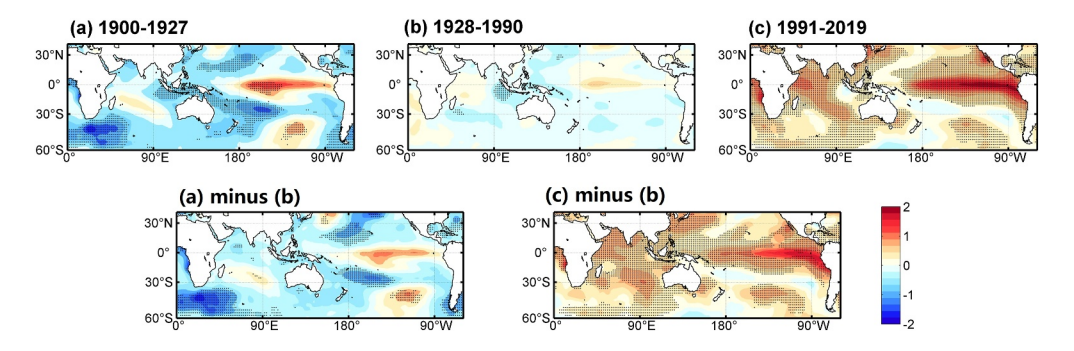


Figure 7. Composite Sea surface temperature anomalies (SSTA, unit: °C) in September–January for the positive Indian Ocean Dipole events in different periods. (a) and (c) are the high-relationship periods of 1900–1927 and 1991–2019; (b) the low-relationship period of 1928–1990. The bottom panels are the difference between high- and low-relationship periods. The dots indicate the statistical significance exceeding the 95% confidence level.

WANG ET AL. 9 of 12

21698996, 2025, 18, Downloaded from https://agupubs.onlinelibrary.wiley.com/doi/10.1029/2025JD043936 by Lanzhou University, Wiley Online Library on [05/11/2025]. See the Terms and Conditions (https://onlinelibrary.wiley.com/term

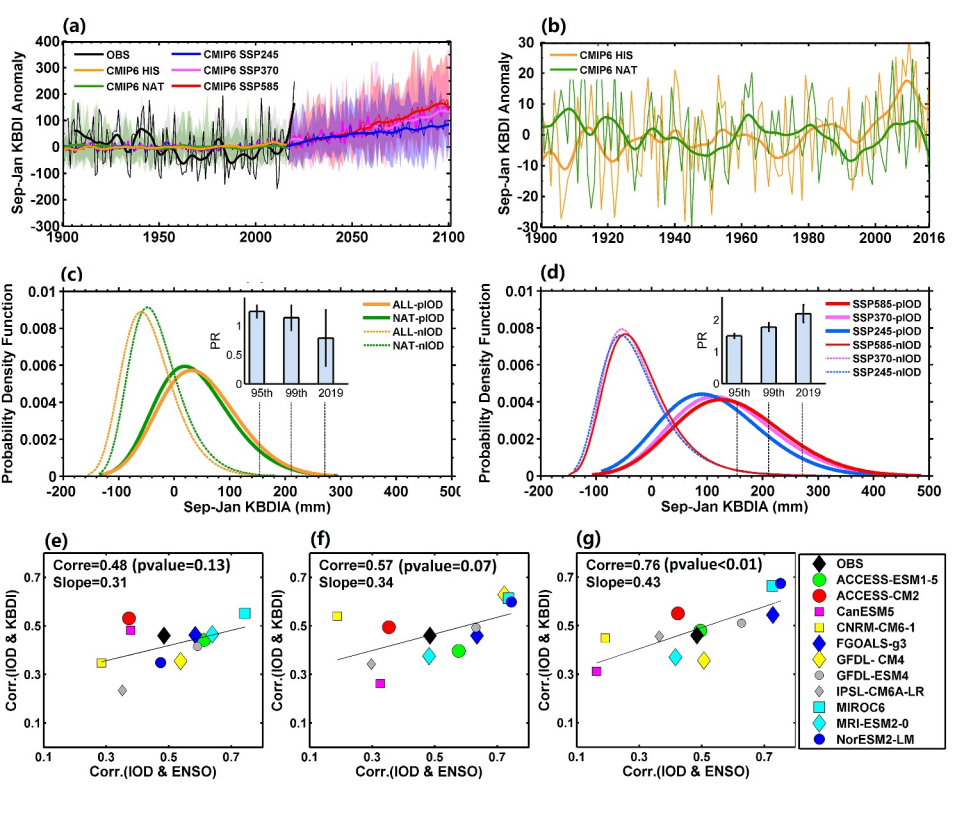


Figure 8. KBDI performances in CMIP6 simulations. (a) Temporal variation of September–January KBDI anomalies. The thin black line is the observations from Australia's Bureau of Meteorology, with the thick line showing its 11-year running mean. CMIP6 ensemble means are shown for: The thin orange (green) and blue (purple and red) solid lines are the CMIP6 ensemble mean from the historical-ALL (historical-NAT) and SSP245 (SSP370 and SSP585) projections. The shading denotes the 95% confidence intervals of 11 models. The partial enlarged detail for the historical simulations is shown in (b). (c) Probability density functions (PDFs, curves) for September–January southeastern Australia KBDI in different Indian Ocean Dipole (IOD) events, from CMIP6 simulations under all (ALL, orange) and natural only (NAT, green) forcings, and the Probability Ratio (PR, bars) of the 95th percentile, 99th percentile and 2019–20 mega fire thresholds in historical-ALL versus historical-NAT simulations. (d) Projected PDFs but for SSP245, SSP370 and SSP585 scenarios. PR values (bars) quantify the probability amplification of exceeding extreme thresholds in SSP585 versus SSP245. (e) The inter-model relationship between the correlation of IOD and ENSO (*x*-axis) and the correlation of IOD and KBDI (*y*-axis) from the historical-ALL. Panels (f) and (g) are same as (e), but for the second half of 21st century under SSP245 and SSP585 projections, respectively. The pairs of observations used are listed in the legend.

anthropogenic warming, the effect of IOD/ENSO relationship on IOD's climatic impact is expected to significantly intensify in the future, with the correlation rising from 0.48 for 1900–2014 under historical-ALL to 0.76 for 2050–2100 under SSP585.

4. Discussion and Conclusion

Our findings demonstrate that the climatic effects of pIOD have enhanced in recent decades, likely due to the increasingly coupling between the IOD and ENSO, as well as more frequent concurrent of pIODs with El Niño events. Quantitatively, our analysis using CMIP6 multi-model ensembles predicts a substantial future increase in wildfire potential: the probability of severe bushfire events (above the 95th percentile) driven by pIOD is projected to rise by approximately 50% ($\pm 8\%$), and the likelihood of very extreme events akin to the 2019-2020 mega-fires could increase from 4% to 10% under SSP585 scenarios. Although SSP585 provides an upperbound estimate, we emphasize SSP370 as the more plausible high-emission benchmark. Under this scenario, the probability of severe (extreme) pIOD-driven bushfires is projected to reach 37% (20%) by 2100, a notable increase from the 28% (13%) projected under SSP245. Although CMIP6 models were selected based on performance in simulating Australian climate (Grose et al., 2020), inter-model spread in precipitation extremes contributes to uncertainty in projected fire risk (Figure 8d). We mitigated this via ensemble averaging and

WANG ET AL. 10 of 12

bootstrapping, yet low-likelihood extremes (e.g., >99th percentile KBDI) remain sensitive to the model structure. Furthermore, the probability of extreme precipitation deficits during pIOD years has nearly doubled since 1991, from 11.2% to 21.6%. These projections underscore a significant escalation in fire weather risk in the region. Climate change is expected to make fire-prone weather more prevalent in SEA. By the end of the 21st century, bushfire risk over SEA associated with pIOD is projected to increase significantly.

Cai et al. (2013, 2014) highlighted that under greenhouse warming, the equatorial Indian Ocean is evolving toward a climatologically stronger west-minus-east temperature gradient and intensified easterly winds, conditions more conductive to producing more frequent extreme pIOD events in the future. With the projected dramatic increase in extreme pIOD occurrences and their amplified climatic effects, strategic precautions must be taken to mitigate the likely rise in devastating fire weather events across affected regions.

Moreover, the increasing frequency and severity bushfires contribute substantial carbon dioxide emissions to the atmosphere, exacerbating the occurrence of extreme hot and dry conditions and further elevating bushfire risk in SEA. This forms a positive feedback loop, where intensified fire activity and climate change mutually reinforce one another, escalating the threat of more frequent and severe bushfire events.

Although this study provides insights into the mechanisms behind the enhancing linkage between pIOD events and Australia bushfire risk, further research is crucial. Future work need to conduct a comprehensive investigation into the potential causes of these enhanced climate effects associated with pIOD events. This includes exploring how interdecadal climate modes such as the Pacific decadal oscillation and the Atlantic multidecadal oscillation, as well as anthropogenic climate change, might modulate the climate impacts of IOD and its interaction with ENSO. Understanding how these factors influence the strength and behavior of IOD is very crucial for refining its role as a key predictive factor in Austrialia's seasonal fire forecast. For instance, during periods where pIOD effects are significantly enhanced, IOD will be emphasized as a primary predictor. Conversely, under condition of weaker climate influence or specific interdecadal configurations, its contribution could be down-weighted or even omitted. This adaptive strategy aims to identify the optimal combination of climate predictors across various warming backgrounds and interdecadal regimes, thereby improving the accuracy and reliability of seasonal fire risk forecasts.

Data Availability Statement

Meteorological variables, including daily maximum and minimum air temperatures ($T_{\rm max}$ and $T_{\rm min}$), were obtained from the Australian Gridded Climate Data set (AGCDv2; https://thredds.nci.org.au/thredds/catalog/catalogs/zv2/agcd/agcd.html). Modis active fire data (Collection 6) was downloaded from https://firms.modaps.eosdis.nasa.gov/download/. The NOAA Precipitation Reconstruction (PREC) are available from https://www.psl.noaa.gov/data/gridded/data.prec.html. The outgoing longwave radiation (OLR) data from the NCEP-NCAR Reanalysis 1 was downloaded from https://psl.noaa.gov/data/gridded/data.ncep.reanalysis.html. The Extended Reconstruction of SST (ERSSTv5) data set was sourced from the website https://climatedataguide.ucar.edu/climate-data/sst-data-noaa-extended-reconstruction-ssts-version-5-ersstv5. The CMIP6 products can be accessed at https://esgf-node.llnl.gov/search/cmip6/.

Acknowledgments

We acknowledge the World Climate Research Programme's Working Group on Coupled Modeling, which is responsible for CMIP. We acknowledge professor Cai Wenjun for his invaluable suggestions throughout this research. This work was jointly supported by the National Science Foundation of China (4252200766 and 42475023).

References

- Abram, N. J., Henley, B. J., Sen Gupta, A., Lippmann, T. J. R., Clarke, H., Dowdy, A. J., et al. (2021). Connections of climate change and variability to large and extreme forest fires in southeast Australia. *Communications Earth & Environment*, 2, 1–17. https://doi.org/10.1038/s43247-020-00065-8
- Ashok, K., Guan, Z., & Yamagata, T. (2003). Influence of the Indian Ocean dipole on the Australian winter rainfall. *Geophysical Research Letters*, 30(15), 1821. https://doi.org/10.1029/2003GL017926
- Boer, M. M., Resco de Dios, V., & Bradstock, R. A. (2020). Unprecedented burn area of Australian mega forest fires. *Nature Climate Change*, 10(3), 171–172. https://doi.org/10.1038/s41558-020-0716-1
- Cai, W., Cowan, T., & Raupach, M. (2009). Positive Indian Ocean dipole events precondition southeast Australia bushfires. *Geophysical Research Letters*, 36(19), L19710. https://doi.org/10.1029/2009GL039902
- Cai, W., Santoso, A., Wang, G., Weller, E., Wu, L., Ashok, K., et al. (2014). Increased frequency of extreme Indian Ocean dipole events due to greenhouse warming. *Nature*, 510(7504), 254–258. https://doi.org/10.1038/nature13327
- Cai, W., Van Rensch, P., Cowan, T., & Hendon, H. H. (2011). Teleconnection pathways of ENSO and the IOD and the mechanisms for impacts on Australian rainfall. *Journal of Climate*, 24(15), 3910–3923. https://doi.org/10.1175/2011JCLI4129.1
- Cai, W., Zheng, X. T., Weller, E., Collins, M., Cowan, T., Lengaigne, M., et al. (2013). Projected response of the Indian Ocean dipole to greenhouse warming. *Nature Geoscience*, 6(12), 999–1007. https://doi.org/10.1038/ngeo2009

WANG ET AL. 11 of 12

- Chen, M., Xie, P., Janowiak, J. E., & Arkin, P. A. (2002). Global land precipitation: A 50-yr monthly analysis based on gauge observations [Dataset]. *Journal of Hydrometeorology*, 3, 249–266. https://doi.org/10.1175/1525-7541(2002)003<0249:GLPAYM>2.0.CO;2
- Coles, S., Bawa, J., Trenner, L., & Dorazio, P. (2001). An introduction to statistical modeling of extreme values. Springer.
- Deb, P., Moradkhani, H., Abbaszadeh, P., Kiem, A. S., Engström, J., Keellings, D., & Sharma, A. (2020). Causes of the widespread 2019–2020 Australian bushfire season. *Earth's Future*, 8(11), e2020EF001671. https://doi.org/10.1029/2020ef001671
- Di Virgilio, G., Evans, J. P., Clarke, H., Sharples, J., Hirsch, A., & Hart, M. (2020). Climate change significantly alters future wildfire mitigation opportunities in southeastern Australia. *Geophysical Research Letters*, 47(15), e2020GL088893. https://doi.org/10.1029/2020GL088893
- Di Virgilio, G., Ji, F., Tam, E., Nishant, N., Evans, J. P., Thomas, C., et al. (2022). Selecting CMIP6 GCMs for CORDEX dynamical downscaling: Model performance, independence, and climate change signals. *Earth's Future*, 10(4), e2021EF002625. https://doi.org/10.1029/2021EF002625
- Dowdy, A. J., Mills, G. A., Finkele, K., & de Groot, W. (2009). Australian fire weather as represented by the McArthur forest fire danger index and the Canadian forest fire weather index. CAWCR Technical Report, 10, 84. http://www.bushfirecrc.com/sites/default/files/managed/resource/ctr_010.pdf
- Du, J., Wang, K.-C., & Cui, B.-S. (2021). Attribution of the extreme drought-related risk of wildfires in spring 2019 over Southwest China. Bulletin of the American Meteorological Society, 102(1), S83–S90. https://doi.org/10.1175/bams-d-20-0165.1
- Evans, A., Jones, D., Smalley, R., & Lellyett, S. (2020). An enhanced gridded rainfall analysis scheme for Australia [Dataset]. *Australian Bureau of Meteorology*, 66, 55–67. http://www.bom.gov.au/research/publications/researchreports/BRR-041.pdf
- Eyring, V., Bony, S., Meehl, G. A., Senior, C. A., Stevens, B., Stouffer, R. J., & Taylor, K. E. (2016). Overview of the coupled model inter-comparison project phase 6 (CMIP6) experimental design and organization [Dataset]. *Geoscientific Model Development*, 9(5), 1937–1958. https://doi.org/10.5194/gmd-9-1937-2016
- Fischer, E. M., & Knutti, R. (2015). Anthropogenic contribution to global occurrence of heavy-precipitation and high-temperature extremes. Nature Climate Change, 5(6), 560–564. https://doi.org/10.1038/nclimate2617
- Gannon, C. S., & Steinberg, N. C. (2021). A global assessment of wildfire potential under climate change utilizing Keetch-Byram drought index and land cover classifications. Environmental Research Communications, 3(3), 035002. https://doi.org/10.1088/2515-7620/abd836
- Giglio, L., Schroeder, W., & Justice, C. O. (2016). The collection 6 MODIS active fire detection algorithm and fire products [Dataset]. Remote Sensing of Environment, 178, 31–41. https://doi.org/10.1016/j.rse.2016.02.054
- Grose, M. R., Narsey, S., Delage, F. P., Dowdy, A. J., Bador, M., Boschat, G., et al. (2020). Insights from CMIP6 for Australia's future climate. Earth's Future, 8(5), e2019EF001469. https://doi.org/10.1029/2019EF001469
- Grose, M. R., Narsey, S., Trancoso, R., Mackallah, C., Delage, F., Dowdy, A., et al. (2023). A CMIP6-based multi-model downscaling ensemble to underpin climate change services in Australia. Climate Services, 30, 100368. https://doi.org/10.1016/j.cliser.2023.100368
- Huang, B., Thorne, P. W., Banzon, V. F., Boyer, T., Chepurin, G., Lawrimore, J. H., et al. (2017). Extended reconstructed sea surface temperature, version 5 (ERSSTv5): Upgrades, validations, and intercomparisons [Dataset]. *Journal of Climate*, 30(20), 8179–8205. https://doi.org/10.1175/JCLI-D-16-0836.1
- Janis, M., Johnson, M. B., & Forthun, G. (2002). Near-real time mapping of Keetch-Byram drought index in the south-eastern United States. International Journal of Wildland Fire, 11(4), 281–289. https://doi.org/10.1071/WF02013
- Kalnay, E., Kanamitsu, M., Kistler, R., Collins, W., Deaven, D., Gandin, L., et al. (1996). The NCEP/NCAR 40-Year reanalysis project [Dataset]. Bulletin of the American Meteorological Society, 77(3), 437–471. https://doi.org/10.1175/1520-0477(1996)077<0437:TNYRP>2.0.CO;2
- Keetch, J., & Byram, O. M. (1968). A drought index for forest fire control (Vol. 38). US Department of Agriculture, Forest Service.
- Lucas, C., Hennessy, K., Mills, G., & Bathols, J. (2007). Bushfire weather in southeast Australia: Recent trends and projected climate change impacts.
- Nolan, R. H., Boer, M. M., Collins, L., Resco de Dios, V., Clarke, H., Jenkins, M., et al. (2020). Causes and consequences of eastern Australia's 2019–2020 season of mega-fires. *Global change boil*, 6(3), 1039–1041. https://doi.org/10.1111/gcb.14987
- Plucinski, M. P., Tartaglia, E., Huston, C., Stephenson, A. G., Dunstall, S., McCarthy, N. F., & Deutsch, S. (2023). Exploring the influence of the Keetch–Byram drought index and McArthur's drought factor on wildfire incidence in Victoria, Australia. *International Journal of Wildland Fire*, 33(1), WF23073. https://doi.org/10.1071/WF23073
- Ren, H.-L., Zou, J. Q., & Deng, Y. (2019). Statistical predictability of Niño indices for two types of ENSO. Climate Dynamics, 52(9–10), 5361–5382. https://doi.org/10.1007/s00382-018-4453-3
- Saji, N. H., Goswami, B. N., Vinayachandran, P. N., & Yamagata, T. (1999). A dipole mode in the tropical Indian Ocean. *Nature*, 401(6751), 360–363. https://doi.org/10.1038/43854
- Salehnia, N., Zare, H., Kolsoumi, S., & Bannayan, M. (2018). Predictive value of Keetch-Byram drought index for cereal yields in a semi-arid environment. *Theoretical and Applied Climatology*, 134(3), 1005–1014. https://doi.org/10.1007/s00704-017-2315-2
- Sun, C., Li, J., & Ding, R. (2016). Strengthening relationship between ENSO and western Russian summer surface temperature. *Geophysical Research Letters*, 43(2), 843–851. https://doi.org/10.1002/2015GL067503
- Ummenhofer, C. C., England, M. H., McIntosh, P. C., Meyers, G. A., Pook, M. J., Risbey, J. S., et al. (2009). What causes southeast Australia's worst droughts? *Geophysical Research Letters*, 36(4), L04706. https://doi.org/10.1029/2008GL036801
- Van Oldenborgh, G. J., Krikken, F., Lewis, S., Leach, N. J., Lehner, F., Saunders, K. R., et al. (2021). Attribution of the Australian bushfire risk to anthropogenic climate change. Natural Hazards and Earth System Sciences, 21(3), 941–960. https://doi.org/10.5194/nhess-21-941-2021
- Wang, G., & Cai, W. (2020). Two-year consecutive concurrences of positive Indian Ocean dipole and Central Pacific El Niño preconditioned the 2019/2020 Australian "black summer" bushfires. Geoscience Letters, 7(1), 19. https://doi.org/10.1186/s40562-020-00168-2
- Wang, S., Yuan, X., & Wu, R. (2019). Attribution of the persistent spring–summer hot and dry extremes over Northeast China in 2017. Bulletin of the American Meteorological Society, 100(1), S85–S89. https://doi.org/10.1175/BAMS-D-18-0120.1
- Yuan, X., Wang, & Hu, Z. Z. (2018). Do climate change and El Niño increase likelihood of Yangtze River extreme rainfall? Bulletin of the American Meteorological Society, 99, S113–S117. https://doi.org/10.1175/BAMS-D-17-0089
- Zhang, W., Mao, W., Jiang, F., Stuecker, M. F., Jin, F.-F., & Qi, L. (2021). Tropical Indo-Pacific compounding thermal conditions drive the 2019 Australian extreme drought. *Geophysical Research Letters*, 48(2), e2020GL090323. https://doi.org/10.1029/2020GL090323

WANG ET AL. 12 of 12